

Special issue article



A novel approach to tire parameter identification

Proc IMechE Part D:

J Automobile Engineering
2019, Vol. 233(1) 55–72

© IMechE 2018
Article reuse guidelines:
sagepub.com/journals-permissions
DOI: 10.1177/0954407018771253
journals.sagepub.com/home/pid

Hojong Lee and Saied Taheri

Abstract

Since they are believed to provide more reliable and accurate tire contact parameters, intelligent tires have been widely studied for the purpose of the performance enhancement of the vehicle control systems such as anti-lock breaking system and the electronic stability program. Moreover, it is also expected that intelligent tires can be utilized to analyze tire dynamic response, taking into consideration that the measurements from the sensors inside the tire would contain considerable information on tire behavior in real driving scenarios. In this work, the tire physical characteristics related to in-plane dynamics of the tire, such as stiffness of the belt and sidewall and contact pressure distribution, were identified based on the combination of strain measurements and a flexible ring tire model. The radial deformation of the tread band was directly obtained from strain measurements based on the strain-deformation relationship. Tire parameters were identified by fitting the radial deformations from the flexible ring model to those derived from strain measurements. This approach removed the complex and repeated procedure to satisfy the contact constraints between the tread and the road surface in the traditional ring model. For validation purposes, circumferential strains were measured for three different tires on a Flat-Trac indoor test rig. And then, circumferential contact pressures and tire parameters were estimated based on these measurements. Identification using only model-based methods was conducted and comparison was made to the measured contact patch shapes. The comparison among identification methods and measurements shows good agreement. The proposed method of utilizing intelligent tire fused with physical tire model is expected to provide another tool to investigate tire characteristics. Moreover, tire properties identified using intelligent tires could be more closely linked to vehicle performance.

Keywords

Intelligent tire, sensor, strain, parameter identification, tire model

Date received: 16 September 2017; accepted: 5 March 2018

Introduction

Sensor embedded tires, the so-called intelligent tires, have been widely researched in the tire and automotive industries because they are believed to provide more reliable and exact tire information to vehicle active control systems like anti-lock braking system (ABS) and Electronic Stability Program (ESP) (), than traditional indirect estimation methods. Thus, the improvement of control performance is expected with the help of intelligent tire system. In intelligent tire systems, deformations, and accelerations are measured at locations of interest with corresponding sensors. For these measurements to contain abundant information about the tire contact characteristics, the measured locations are determined as close to the contact area as possible. To secure the durability of sensors, they are usually attached to the innerliner over the tread portion than inserted into the tire layers.

To obtain meaningful tire parameters from sensor measurements, different sorts of estimation algorithms have been tried in previous research. Most of them are based on the simple regression methods, where tire parameters are considered as estimated outputs and features of the measured signals serve as the inputs.

Table 1 lists the literature showing the estimated tire parameters and corresponding predictors. Details can be found in the referred literature. These methods are expected to provide more reliable tire parameters using

Center for Tire Research (CenTiRe), Department of Mechanical Engineering, Virginia Polytechnic Institute and State University, Blacksburg, VA, USA

Corresponding author:

Hojong Lee, Center for Tire Research (CenTiRe), Department of Mechanical Engineering, Virginia Polytechnic Institute and State University, 635 Prices Fork Road—MC 0238, Blacksburg, VA 24060, USA. Email: lhojong@vt.edu

Table 1. Review of the previous work on intelligent tires.

Estimated tire parameter	Predictor extracted from sensor measurement			
Contact length	Peak-to-peak distance of acceleration or strain rate 1,2			
Vertical force (F_z)	Peak-to-peak distance of acceleration or strain rate ^{1,2} Estimated Contact length ^{1–6}			
	Compressive peak or tensile peak of strains ^{6–8} Integral of circumferential strains within contact ⁹			
Slip angle and lateral forces (F_y)	Differences in contact length or strains at inner and outer part of cornering contact patch (more than a pair of sensors were used). ^{1–6}			
Longitudinal force (F_x)	Difference between the leading and trailing contact angle. (Wheel encoder sensor is required). ¹⁰			
	Difference in compressive peaks of lateral strain, between before and after contact patch. ⁶			

advanced statistical methods or machine learning algorithms.

Besides the main applications of intelligent tire mentioned previously, it is also promising to use sensed measurements from intelligent tire for the analysis of tire from the point of view of the tire design engineer. This is because the accelerations or strains measured near the contact patch have ample information on tire characteristics. To achieve this goal, well-established theories in tire models can be incorporated into the process of identification of tire characteristics. A few previous researchers have adopted this approach to estimate tire parameters. Erdogan et al. 11 obtained the carcass lateral profile by double integrating the acceleration in the lateral direction measured at the innerliner and introduced the lateral carcass deflection model¹² to estimate the lateral force and the self-aligning moment. These estimated parameters were finally used as inputs to the brush type tire model to obtain the friction coefficient. This work was advanced further by Hong et al., 13 who applied this method to real-world scenarios by taking the tire deformation effects on measured acceleration into consideration. Matsuzaki et al.8 also used the double integral of lateral acceleration to obtain the lateral profile of carcass line, which was correlated with lateral force. In these works, identification of the lateral deformation was used for the estimation of the lateral force with the assumption that the lateral stiffness of tire is known.

In this article, a modified flexible ring model is introduced to identify the characteristics related to in-plane dynamics of the tire. As the name of "flexible ring" implies, this model represents the tread band of the tire as a flexible ring, which is supported by the viscoelastic sidewall elements (between the ring and the wheel). Flexible ring models are widely used to analyze the vibration properties as well as to solve the circumferential contact problems between the tire and the road surface. As to the contact problem, tread elements should be included to account for the boundary conditions between the tire and the road surface. Figure 1 illustrates a general flexible ring model of a tire-wheel system, which include almost every model parameter of this model concept and tread elements as well. Model

parameters are listed with description at the right hand side in the figure.

Yamagishi and Jenkins^{14,15} and Jenkins¹⁶ studied the circumferential contact problem of the belted radial tire by taking into account the tread rubber as distributed springs along the outer layer of the circular ring. In their study, they assumed the contact angles to be known, whereas they are usually unknown in real applications. The ring was separated into the free region and the contact region. Governing equations are solved separately for each region by finding numerical solutions of differential equations. The arbitrary constants were determined by symmetry conditions of the static tire and continuity conditions at contact edges. There were convergence issues, so they used a singular perturbation method to get the approximate solution. Gong¹⁷ used the same boundary conditions but solved the contact problem with a more advanced ring model which includes the circumferential stiffness and damping of the sidewall, and dynamic effects of a free rolling tire on the flat road. Rather than solving the equation using conventional methods, modal expansion method was used considering the flexible ring as one unit. After considerable numerical manipulations, he calculated the ring deformation and the contact pressure distribution under the assumption that the contact angles were known. For the case of unknown contact angles, other information such as the vertical deformations or loads were used instead and the solution process was repeated until one of the contact angles met the required boundary condition at the corresponding edge. And then, another iteration process was conducted to find the other contact angle while keeping the previously found contact angle as constant. It needs to be pointed out that finding contact angles sequentially is likely to make some error because the fixed contact angle from the first iteration should be affected when the other contact angle varies through the second iteration process. In other words, they need to be determined simultaneously. Kim and Savkoor¹⁸ introduced a more realistic compatibility condition for the tread elements for the circumferential contact problems of the free rolling tire on the flat surface. He introduced the shear deformation of the tread and distributed moments along the

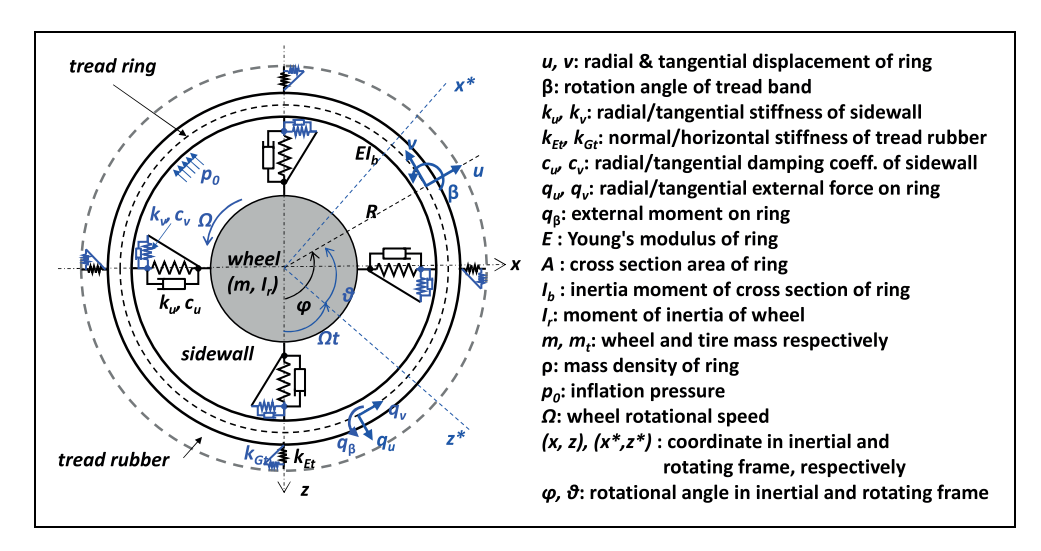


Figure 1. General flexible ring model of a tire-wheel system.

beam axes due to the shear deformation of the tread. Therefore, the boundary condition became complex and nonlinear, making it impossible to find an analytical solution. So, he introduced a two-step solution: first, the boundary conditions were linearized and approximate solutions were found similar to Gong's approach. Second, exact solutions were obtained through iterative process from the approximate solutions using the exact, non-linear compatibility conditions of the tread.

As was shown, solving the equations of the motion for the flexible ring model while satisfying the boundary conditions simultaneously is complex with numerical difficulties. Also, it is difficult to obtain some of the model parameters for flexible ring such as the bending stiffness of tread band and sidewall stiffness. Modal analysis has often been used to get the tire parameters and static test results on indoor test rigs are also used. However, conducting the modal tests and interpreting the results for the purpose of parameterization of the tire are challenging especially for the contact problems where the tire is rolling with a finite contact with the road. Also, model parameters obtained from the staticindoor test results may not reflect tire characteristics in the real driving scenario. Moreover, when tread elements are introduced, the tread stiffness should be estimated, which does not exactly correspond to the modulus of the tread rubber but a synthetic value determined by the bending stiffness of the tread band, the rubber modulus as well as some geometrical values such as the tread thickness and the beam width as discussed in Yamagishi and Jenkins.¹⁴

In this article, the contact problem was solved based on the combination of strain gage measurements, finite element modeling (FEM), and the flexible ring model. The rest of the article is organized as follows: Testing method is discussed in the next section, which is followed by the simulation method of the circumferential strains. And then, circumferential contact problems were solved for three different tires by using both of

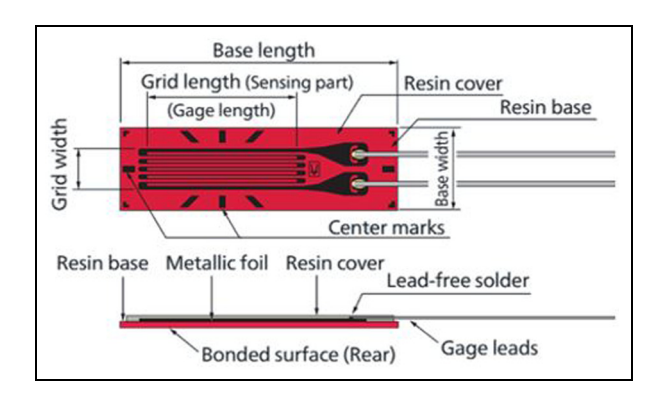


Figure 2. Structure of a foil strain gage.

the suggested method and conventional method for the validation purpose. Discussions and conclusions are given at the end.

Experimental tire testing and data processing

A strain-based intelligent tire was utilized in this research. Types of strain gages are classified into foil strain gages, wire strain gages, semiconductor strain gages, and so on. In this study, foil strain gages were used and their structure is shown in Figure 2.

The foil strain gage has a metal foil on the electric insulator of a thin resin, and gage leads are attached to this foil, as shown in the figure. The strain gage is bonded to the measuring object (tire innerliner in this study) with a dedicated adhesive. Strain occurring on the measuring site is transferred to the strain sensing element via adhesive and the resin base. For accurate measurement, the strain gage and adhesive should be compatible with the measuring material and operating conditions such as temperature, and so on. If an external tensile force or compressive force applied to tire

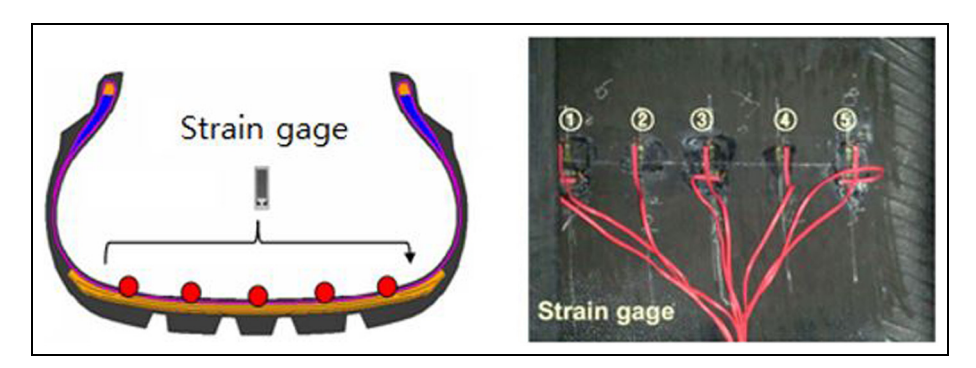


Figure 3. Intelligent tire system with five strain gage: sensor arrangement in the cross section of tire (left) and sensor attachment on the inner liner (right).

increases or decreases, the resistance of the sensing part inside the sensor proportionally increases or decreases. If the resistance R changes by ΔR because of strain ε , the following equation can be written

$$\frac{\Delta R}{R} = K_s \varepsilon \tag{1}$$

The intelligent tire system for this study has five foil strain gages attached to the innerliner, which are equally spaced along the tire axial direction as shown in Figure 3.

All strain gages were oriented in the wheel heading direction to measure circumferential strains. One of the five strain gages should be located at the equator line, because it was revealed that the strain measured at the center can be used to estimate basic tire parameters, especially related to in-plane dynamics of tire. Two pairs of strain gages were attached to off-center positions of the tread to investigate tire parameters for out-of-plane dynamics such as lateral forces and slip angles. However, this research focuses on the identification of in-plane dynamic properties of tires and utilized measurements from the center-located strain gage only. (Study on out-of-plane dynamic features using the same intelligent tire will be published separately.)

Loaded rolling tests were performed with this intelligent tire system on a Flat-Trac test rig. Slip angle sweep tests were conducted; slip angles varies from -5° to $\sim 5^{\circ}$ under five different loads ranging from 25% of the reference load (5669 N) to 175% to measure the force and moment. Since this study aims at characterization of in-plane dynamics, experimental data at zero slip angle was chosen. The inflation pressure and test speed were set to 2.3 bar and 65 km/h, respectively, for all tests. Strain measurements were performed for three different P235/55R19 passenger tires with different belt structures. Since this tire was developed to be provided for original equipment (OE) maker, the reference test load and inflation pressure were set according to OE requirement.

The strains were measured at a fixed frequency of 4800 Hz and measured signals are wirelessly transferred to receivers outside the tire using a transmitter

developed in-house. The measured raw signals showed a wide range of frequencies. High-frequency components above 1 kHz are usually generated by the vibration behavior of tires. This vibration can be caused by the stick-slip motion of the tread while in contact with the road. Thus, these high-frequency components of signals can give information on the level of friction and the type of road surface as discussed in literatures. However, this research focuses on the estimation of overall tire deflections rather than frictional phenomena in micro scale. Therefore, the signals were filtered using a low pass filter with a frequency of 400 Hz. This low pass filter makes sure signals have predominant peak while preserving information as much as possible.

Figure 4 shows the filtered strain time history of the straight rolling tire at the reference test load. Since the circumferential strains typically have two successive compressive peaks before and after the contact region, they can be used to identify one rotation of the tire. The peak identification algorithm was developed and maximum compressive and tension peaks were marked as solid circles in the graph shown in Figure 4.

Since the wheel rotational speed and the test speed are known, strain histories can be obtained as a function of rotation angle. This conversion is only possible when there is no longitudinal slip as in the case of this test. Figure 5 shows strain measurements as a function of rotation angle for different test loads ((a) of Figure 4) and strain rates, i.e. the time rate of change of strain ((b) of Figure 4). The first and second peaks of strain rate are known to correspond to contact angles at the leading and trailing edges of the contact patch, respectively.2 When the tread elements enter and exit the contact region, they undergo sudden deformation which features maximum and minimum peaks in the strain rate. Thus, the peak-to-peak distance in the strain rate is indicative of contact length. Peaks of strain rate and corresponding points in the strain are marked as solid circles in both graphs. It can be seen from the graphs that as test load increases, the contact length, that is, peak-to-peak distance in the strain rate, also increases.

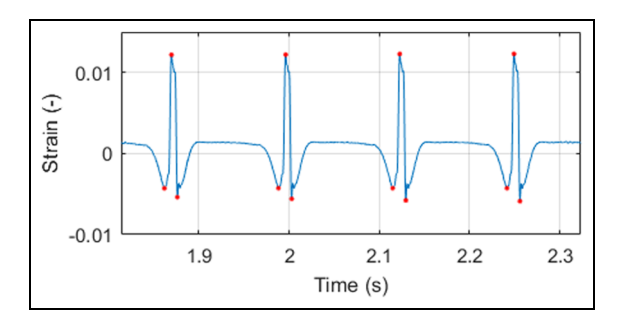


Figure 4. Time history of the measured circumferential strain at innerliner center.

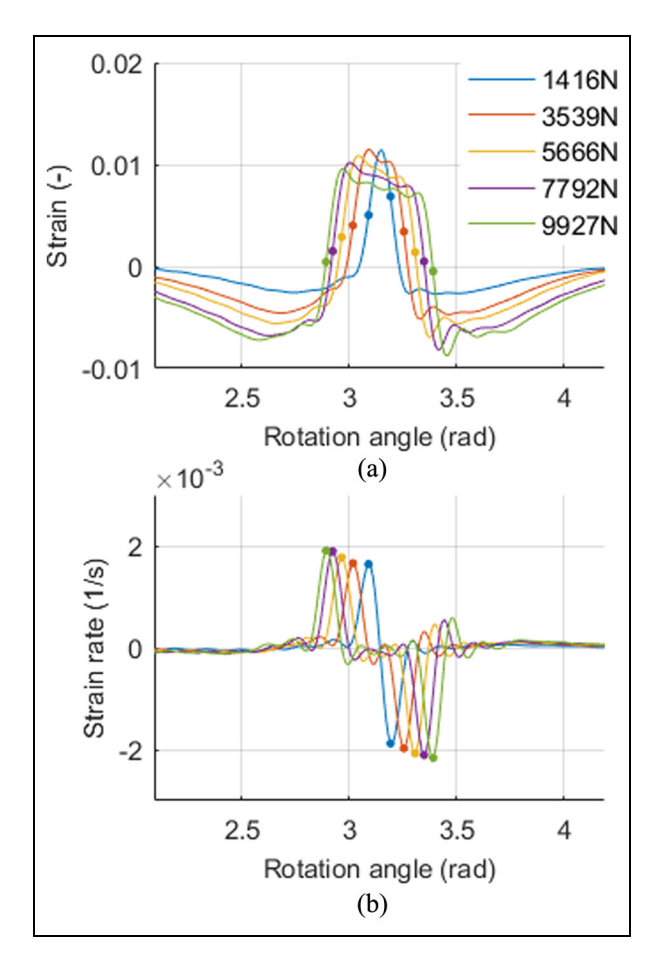


Figure 5. (a) Strain and (b) strain rate versus rotational angle under different test loads measured at center innerliner.

Estimation of radial deformation of the tread band using strain measurements

An analytical model is required to simulate the strain at the innerliner of the loaded rolling tire to find theoretical meanings of measured strains. In this research, the flexible ring model is used because it can deliver the in-plane deformation of the tread band. As the name implies, it represents tire tread band as a homogeneous curved beam, where, the tread band consists of steel belts, the carcass, the innerliner, and a part of the tread base. Even though the relationship between the strains

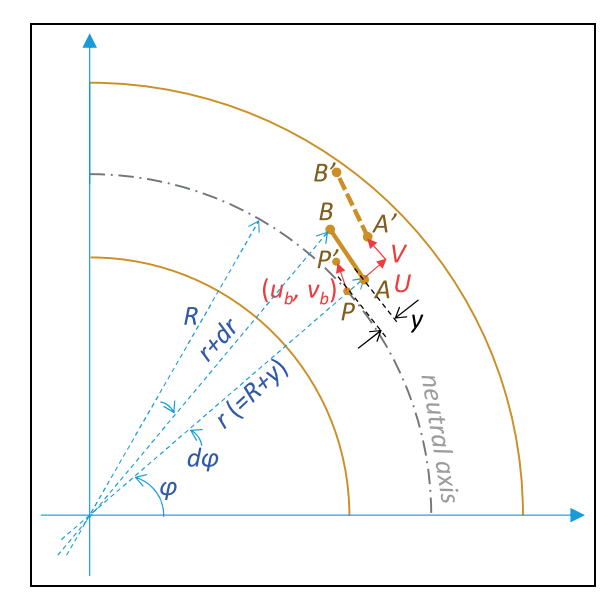


Figure 6. The location of two neighboring points before and after ring deformation.

and the deformation in the homogeneous curved beam is well defined, its validity needs to be confirmed when it is applied to the tread band of a real tire, which is composed of different composite layers. Once, the equation for the deformation–strain relationship is confirmed, the radial deformation of the tread band can be estimated by solving this equation with proper boundary conditions.

The relationship between deformations of tread band and strains at inner liner

Figure 6 illustrates the flexible circular ring. The radius from the center to the neutral axis of the beam is R. During deformation, Point P on the neutral axis at (R, φ) in polar coordinate system moves to P' by u_b and v_b in the radial and tangential directions, respectively. At the same time, two neighboring points A and B located off of the neutral axis move to A' and B', respectively. The location of A and B before deformation is (φ, r) and $(\varphi + d\varphi, r + dr)$, respectively, and A is apart from the neutral axis by y, that is, r = R + y. The deformation of A is defined as U and V in the radial and tangential directions, respectively.

With these definitions, the strains in the element \overline{AB} can be written as the following equation referring ^{17,19}

$$\epsilon_{\varphi} = \frac{1}{r} \left(U + \frac{\partial V}{\partial \varphi} \right) + \frac{1}{2r^2} \left(V - \frac{\partial U}{\partial \varphi} \right) \tag{2}$$

$$\epsilon_r = \frac{\partial U}{\partial r} \tag{3}$$

$$\gamma_{r\varphi} = \frac{1}{r} \frac{\partial U}{\partial \varphi} + \frac{\partial V}{\partial r} - \frac{V}{r} \tag{4}$$

Because a thin beam is considered, Bernoulli-Euler assumption is valid and the cross-section of the beam

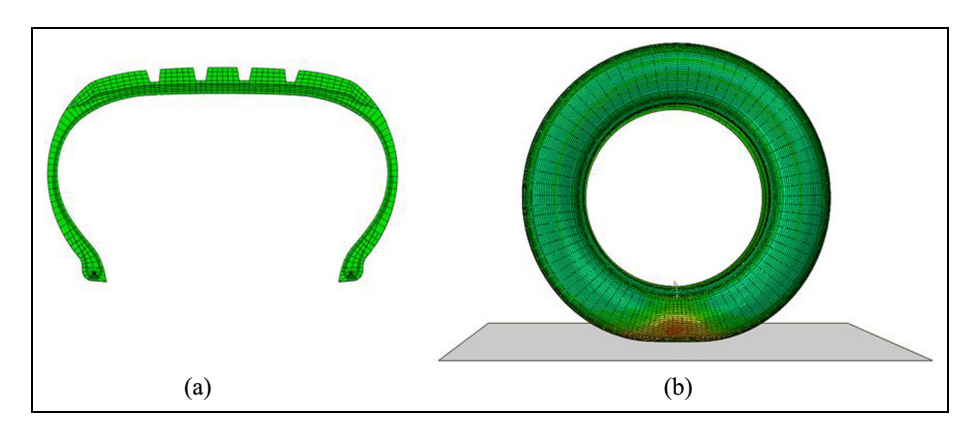


Figure 7. Cross section of (a) FE model and FEM simulation results for circumferential strain when tire is subjected to vertical force on the flat road (b).

remains plane and normal to the neutral axis, which can be written as

$$V(\varphi, y) = v_b(\varphi) + y\beta(\varphi) \tag{5}$$

where β is the rotation angle of the neutral axis.

The radial deformation, U can be approximated by that of neutral axis, u_b . ($U \approx u_b$). Using this assumption and equation (5), the shear strain, $Y_{r\varphi}$ would be expressed in terms of v_b and u_b referring to equation (4). Based on the thin beam assumption, shear strain, $Y_{r\varphi}$ can be neglected (equating equation (4) to zero) giving following relationship for rotation angle, β

$$\beta = \frac{1}{R} \left(v_b - \frac{\partial u_b}{\partial \varphi} \right) \tag{6}$$

Combining equations (2), (5) and (6) gives the final equation for \in_{φ} in terms of v_b and u_b as written is equation (7) (details would be referred to Gong¹⁷)

$$E_{\varphi} = \frac{1}{R} \left(u_b + \frac{\partial v_b}{\partial \varphi} \right) + \frac{y}{R^2} \left(\frac{\partial v_b}{\partial \varphi} - \frac{\partial^2 u_b}{\partial \varphi^2} \right) + \frac{1}{2R^2} \left(\frac{\partial u_b}{\partial \varphi} - v \right)^2$$
(7)

To validate equation (7), FEM simulation was conducted and the graphical deformation is shown in Figure 7.

This simulation was carried out for a 215/60R16 size tire pushed against a flat road surface. The inflation pressure was 2.14 bars and the vertical load of 4765 N was applied. In order to generate the three-dimensional tire model shown in Figure 7, 8-node linear brick, hybrid with constant pressure element was used for rubber and 4-node quadrilateral membrane element with reduced integration is used for carcass and steel belt. The total number of elements of the model is about 120,000, and the circumferential directional element size is varied intentionally in order to reduce the number of element. That is, the finer mesh was adopted at the region of contact with the road surface (bottom part), whereas the mesh was gradually coarsened toward the

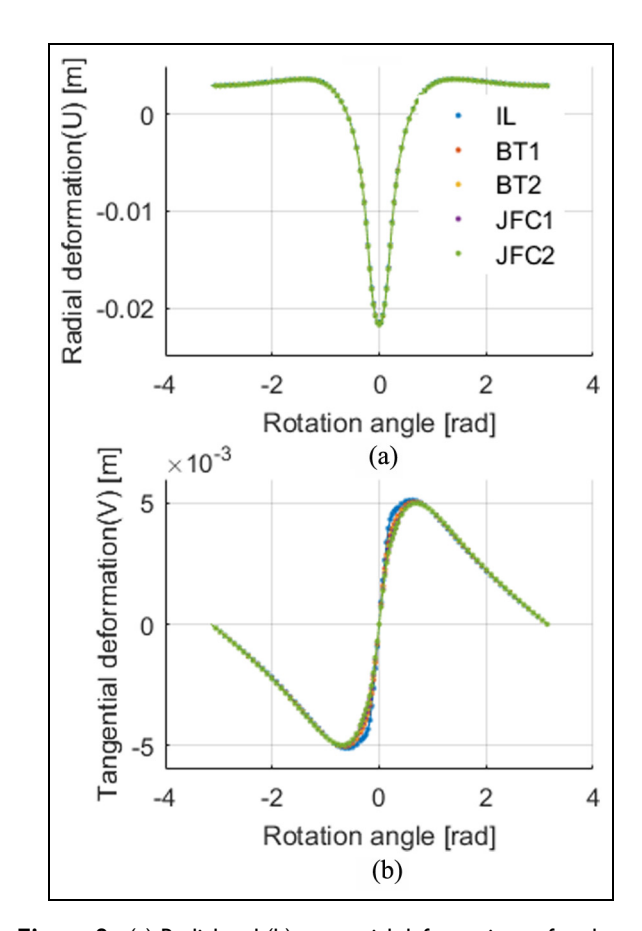


Figure 8. (a) Radial and (b) tangential deformations of each tire layer at center line.

top part. Moreover, a linear elastic material model was applied to steel components such as bead ring and steel belt because these components show a linear elastic behavior under loading, and a linear viscoelastic material model was applied to all types of rubber parts in order to simulate the behavior of rubber more precisely. On the other hand, since textile cords used for the tire show totally different behavior under tension and compression, the tensile and compressive moduli of each textile cord are applied independently for preventing overestimation of textile stiffness under compression.

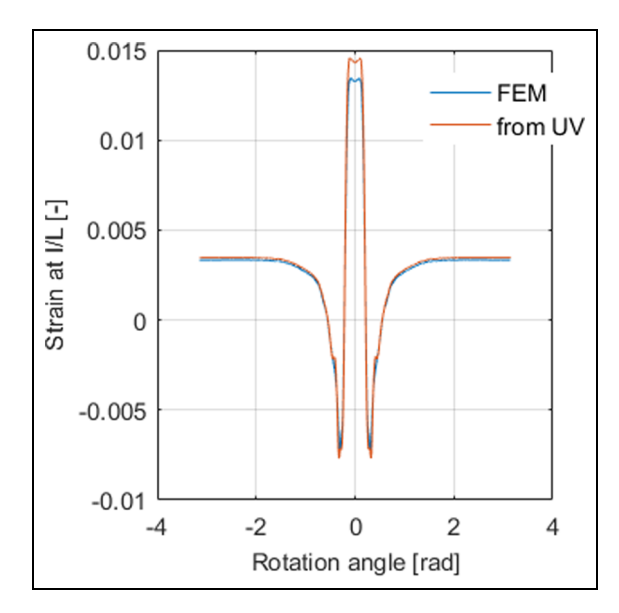


Figure 9. Strains directly from FEM simulation and by calculating from *U*, *V*.

As simulation results, the deformation of each layer was extracted and was converted to corresponding radial-tangential displacements (U, V). Figure 8 shows the radial and tangential deformations of each layer (IL: innerliner, BT1, 2: steel belt 1 and 2, JFC1, 2: reinforcement layer 1 and 2). The radial deformations are identical but tangential deformations differ slightly among layers; inside layers, for example, innerliner, tend to deform more in the contact region.

Figure 9 compares circumferential strains obtained by different methods: one is simulated using FEM and the other is calculated using equation (2) using the deformation of the innerliner (U,V). Though the strain from FEM shows a slightly higher tension in the contact, the calculated one shows almost identical results. So, modeling the tire tread band as a homogeneous ring can represent the circumferential strain of the tire.

Strains at each layer are calculated using their deformations and are shown in Figure 10. The strain at innerliner (IL) shows the high tension within the contact patch and compression arising just before and after contact patch is the same as in the experimental measurements shown in Figure 5. The second reinforcement layer, JFC2 (relatively in the outer part) shows opposite trends. The first and second belts (BT1, BT2, respectively), show the smallest strains overall, which means that they hardly shorten or elongate during the tire deformation. So, their positions can be regarded as the neutral axis of the ring as was also suggested in Yamagishi and Jenkins. ¹⁴ In this article, the first belt is chosen as the neutral axis and its deformations are represented by u_b , v_b (the radial and tangential deformation), respectively.

Using these values and to check the validity of Bernoulli-Euler assumption, the innerliner strain was

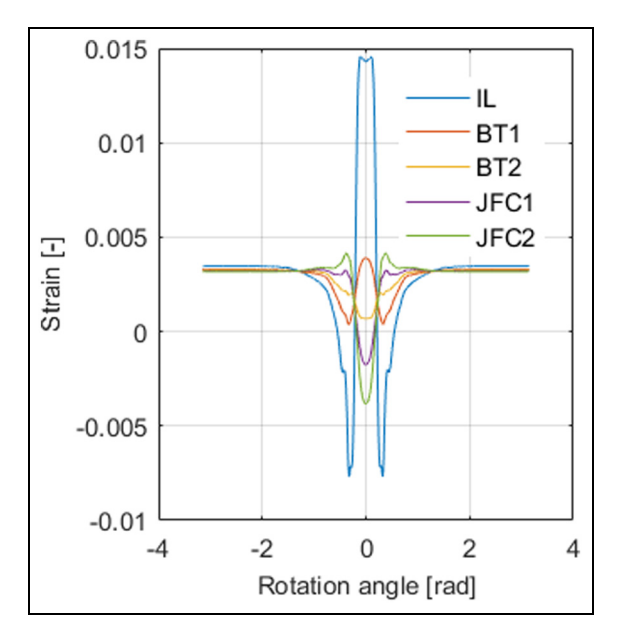


Figure 10. Strains at each layer of tire.

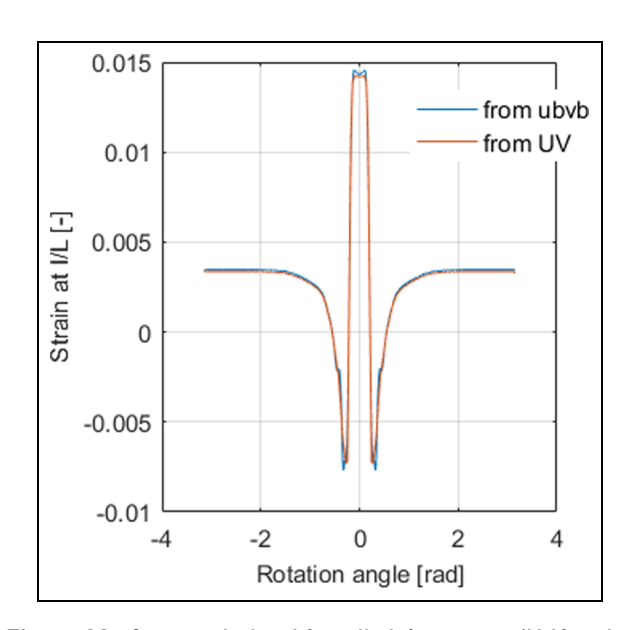


Figure 11. Strains calculated from IL deformations (U, V) and from BTI deformations (u_b , v_b).

calculated using equation (7) and the results are shown in Figure 11. The strain calculated using the deformation of the belt (u_b, v_b) is nearly the same as the one using the deformation of the innerliner (U, V).

Thus, the position of the neutral axis is determined as the location of the first belt line and Bernoulli–Euler assumption is confirmed to be valid for the belted radial tire.

Due to the inflation pressure and the centrifugal force for the rolling tire, usually, tire layers have a small amount of pretension even when they are not in contact with the road surface. This pretension causes

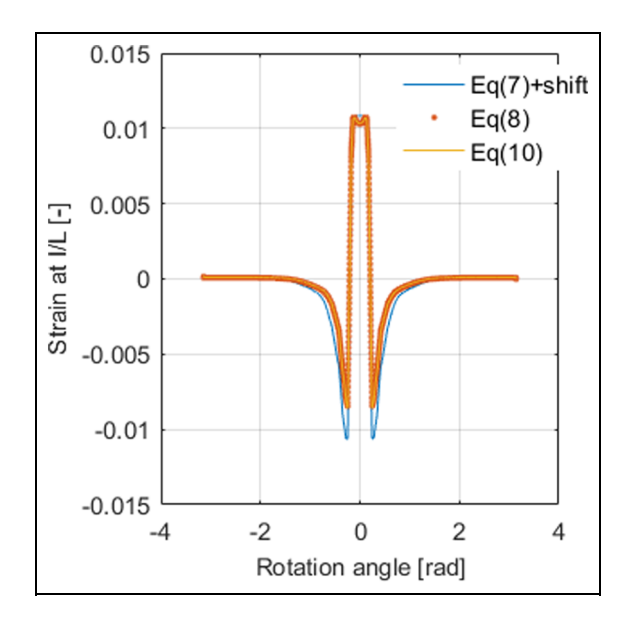


Figure 12. Comparison of strains calculated by using different equations.

the offset in the strain measurement as shown in Figure 4. However, this offset in the measurement is also affected by test sequence, temperature, and sensor drift. Thus, when analyzing strain measurements, this offset is usually removed, which means the circumferential elongation of the tire is not used.

The first and third terms in equation (7) correspond to the circumferential elongation of the ring and second term is induced by its bending motion. So, if just the bending-induced strain is of interest, equation (7) can be reduced to

$$E_{\varphi} = \frac{y}{R^2} \left(\frac{\partial v_b}{\partial \varphi} - \frac{\partial^2 u_b}{\partial \varphi^2} \right) \tag{8}$$

For most of the steel belted radial passenger tires, the inextensibility assumption is also valid, which says that the length of the neutral plane of the ring is constant during deformation. This assumption can be written as

$$\frac{\partial v_b}{\partial \varphi} = -u_b \tag{9}$$

Substituting equation (9) into equation (8) gives the final form of the circumferential strain equation

$$E_{\varphi} = -\frac{y}{R^2} \left(u_b + \frac{\partial^2 u_b}{\partial \varphi^2} \right) \tag{10}$$

Figure 12 compares strains using three different equations. The first strain was calculated by using full strain equation, equation (7), then was shifted such that strain in the free region (opposite to the contact region) is zero and marked as "equation (7) + shift" in the chart. Other strains were calculated using reduced strain equations, equations (8) and (10), and named as corresponding equation numbers in the chart. Some discrepancies are observed in the compression region

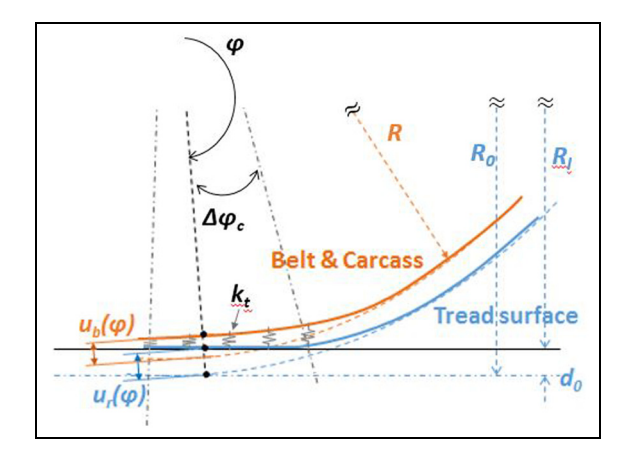


Figure 13. Flexible ring model including tread elements, adapted from Yamagishi and Jenkins. 14

when comparing original strain and approximated ones. However, since this region will not be directly used in the identification process proposed in this article, reduced equations are still considered to be valid. There is no difference between equations (8) and (10) confirming the inextensibility assumption. In this article, equation (8) will be used for the identification of the radial deformation of the belt in the Section 3.2.

Estimation of radial deformation from strain measurement

One of outputs of the flexible ring model is the radial deformation of the tread band especially at the neutral axis. So, if it is possible to estimate the radial deformation of the belt (or neutral axis) from the strains measured at the innerliner, the strain-based intelligent tire can be successfully integrated into the contact problem using the flexible ring model.

The simplest form of the strain-deformation relationship, equation (10), is an ordinary differential equation for the spatial variable φ . This can be simply solved if we know the strain measurement by using finite difference method (FDM) and strain measurements as input. This ordinary differential equation (ODE) can be discretized using FDM such that

$$\frac{y}{(\Delta \varphi R)^2} u_{bi-1} + \frac{y}{R^2} \left(1 - \frac{2}{\Delta \varphi^2} \right) u_{bi} + \frac{y}{(\Delta \varphi R)^2} u_{bi+1} = -E_{\varphi_i}$$
(11)

In this equation, each point "i" corresponds to a measurement point and $\Delta \varphi$ is the incremental step of φ for discretization. Because equation (10) is a second-order ODE, two boundary conditions are required. In this article, these boundary conditions are determined based on the compatibility conditions for tread to contact the flat road, which is suggested by Yamagishi and Jenkins¹⁴ and shown in Figure 13.

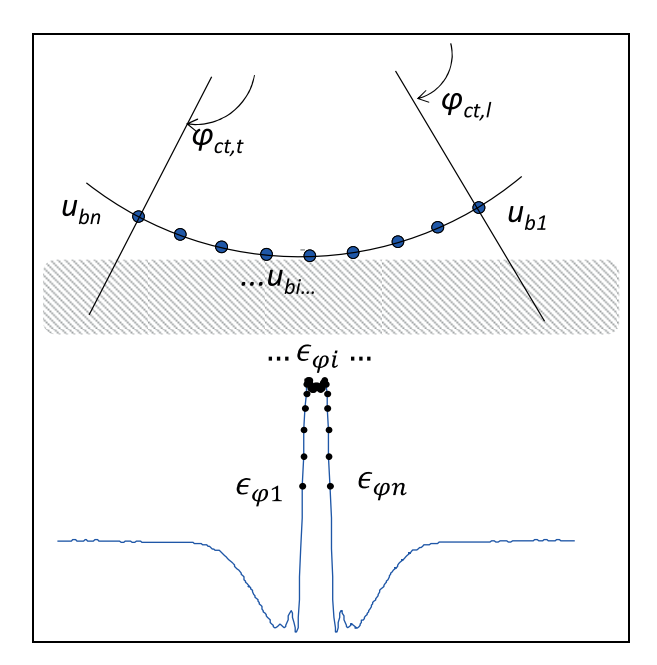


Figure 14. Discretization of radial deformation based at strain-measurement points.

In this concept, the deformed tire against the flat surface is considered and tread elements are modeled as radial springs of which stiffness is k_t . R_0 is the overall radius of the undeformed tire and R_l is the loaded radius. The pressure distribution can be obtained by multiplying tread deformation and tread stiffness (k_t) . The tread deformation can be determined by the difference between the radial deformation of tread band (u_b) and the total deformation of the tire (u_r) , that is, u_b - u_r where u_r is obtained from the loaded tire geometry as shown in the following equation

$$u_r(\varphi) = -\frac{d_0}{\cos(\pi - \varphi)} + R_0 \left(\frac{d_0}{\cos(\pi - \varphi)} - 1\right)$$
(12)

where $d_0 = R_0 - R_l$.

This relationship can be approximated in the linearized form with a high accuracy when d_0 is much smaller than R_0^{-14}

$$u_r(\phi) = -d_0 + R_0(1 - \cos(\pi - \phi)) \tag{13}$$

From the strain rate peak values (refer to Figure 5), the leading and trailing contact angles ($\varphi_{c, l}$, $\varphi_{c, l}$) were identified and the corresponding total radial deformations (u_r) were calculated using equation (13). At both edges of the contact patch, the pressure should be zero, which means the amount of ring deflection (u_b) becomes the same as the total radial deformation of the tire (u_r). Thus, the boundary conditions can be written as shown in equation (14)

$$u_{b}(\varphi_{c,l}) = u_{r}(\varphi_{c,l}) = -d_{0} + R_{0}(1 - \cos(\pi - \varphi_{c,l}))$$

$$u_{b}(\varphi_{c,l}) = u_{r}(\varphi_{c,l}) = -d_{0} + R_{0}(1 - \cos(\pi - \varphi_{c,l}))$$
(14)

As was mentioned previously, in this research, a simple flexible ring model was considered for the static tire subjected to vertical force only. Thus, tread band deformation is symmetrical with respect to the center point of contact patch, and the strain profile at the innerliner should also be symmetrical. However, the pressure distribution of the loaded rolling tire is asymmetrical due to rolling resistance. Thus, the radial deformation and the circumferential strain become asymmetrical, especially in the contact region. To obtain meaningful information on tire characteristics from strains using this static ring model, symmetrical shaped strains are preferred. Therefore, measured strains were approximated to become symmetric using Fourier cosine series expansion.

Equation (15) is the matrix form of the set of linear equations from FDM (equation (11)) for unknown variables, u_{bi} (i = 2 ... n-1)

$$\begin{bmatrix} b & c & 0 & 0 & 0 & \dots & 0 \\ a & b & c & 0 & 0 & \dots & 0 \\ 0 & a & b & c & 0 & \dots & 0 \\ 0 & \dots & \dots & \dots & \dots & \dots & 0 \\ 0 & \dots & \dots & a & b & c & 0 \\ 0 & \dots & \dots & 0 & a & b & c \\ 0 & \dots & \dots & 0 & 0 & a & b \end{bmatrix} \begin{bmatrix} u_{b2} \\ u_{b3} \\ u_{b4} \\ \dots \\ u_{bn-4} \\ u_{bn-3} \\ u_{bn-2} \end{bmatrix}$$

$$= \begin{bmatrix} E_{\varphi 2} - au_{b1} \\ E_{\varphi 2} \\ E_{\varphi 4} \\ \dots \\ E_{\varphi n-4} \\ E_{\varphi n-3} \\ E_{\varphi n-3} \\ E_{\varphi n-3} - au_{bn} \end{bmatrix}$$

$$(15)$$

where u_{bi} are radial deformations of the contact patch corresponding to each measured strain data point. a, b, and c coefficients are determined as

$$a = \frac{y}{(\Delta \varphi R)^2}, b = \frac{y}{R^2} \left(1 - \frac{2}{\Delta \varphi^2} \right), c = \frac{y}{(\Delta \varphi R)^2}$$
 (16)

 u_{b1} and u_{bn} of equation (15) are pre-determined from boundary conditions given by equation (14). This discretization concept is illustrated in Figure 14.

This set of linear equations, equation (15) can be easily solved to find u_{bi} by using a linear solver. The estimated radial deformations are plotted in Figure 15. Notice that the deformation is estimated only within the contact patch since boundary conditions were defined at both contact edges. As test load increases, the radial deformation and the contact length increase as well.

To check the accuracy of the solution, strains were recalculated from the solution (u_i) and compared with Fourier approximations of real measurements. This is shown in Figure 16. Both methods are in agreement with high accuracy.

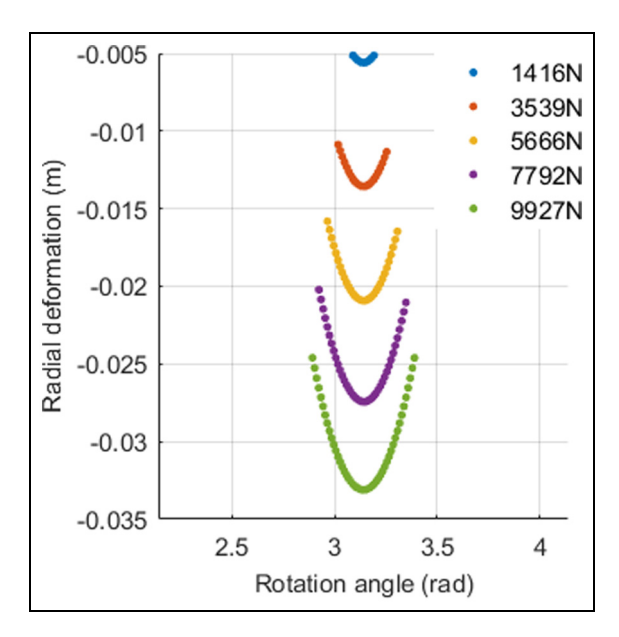


Figure 15. Radial deformations at different vertical loads estimated from strain measurements.

Application of strain measurement for circumferential contact problems

A simple flexible ring model was introduced to be used with the strain measurement and the conventional method for contact problems was reviewed briefly. And then, a newly suggested method for solving the circumferential contact problem is described.

Flexible ring model

In the current study, a simple flexible ring model presented in Kim²⁰ was used to obtain the deformation of the tread band. Figure 17 illustrates a tire model comprising a circular beam and series of radial springs. The circular beam, with radius R, represents the tread band and the radial spring models the sidewall and air pressure. EI_b is the bending stiffness of the circular beam in unit of Nm^2 and K_u is the stiffness per unit length of a radial spring in unit of N/m^2 . A point load P is applied at the bottom of the ring. $u_b(\varphi)$ is the radial deformation and positive sign means a radial-outward deformation. Tread elements were modeled as radial springs with stiffness k_t attached along the ring circumference to deal with the contact problems. Compared with the general flexible ring model shown in Figure 1, this model is limited to a static tire subjected to radial forces only. Moreover, damping effects of sidewall (c_u , c_v in Figure 1) and tangential stiffness of sidewall (k_v) were neglected. These assumptions resulted in the analytical solution without much sacrifice of accuracy in the radial ring deformation.

The force equilibrium diagram is shown in Figure 18 for an infinitesimal element of the ring where Q, N, and M are shear force, normal force and moment, respectively, applied to this beam element.

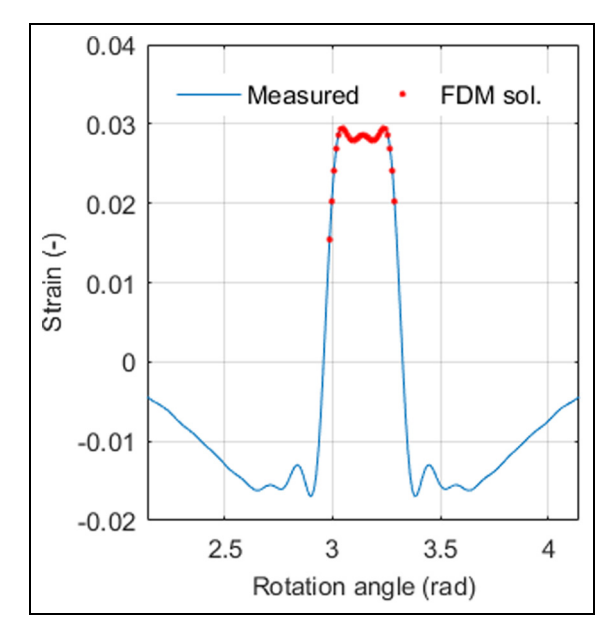


Figure 16. Convergence of FDM solution at F_z = 5666 N.

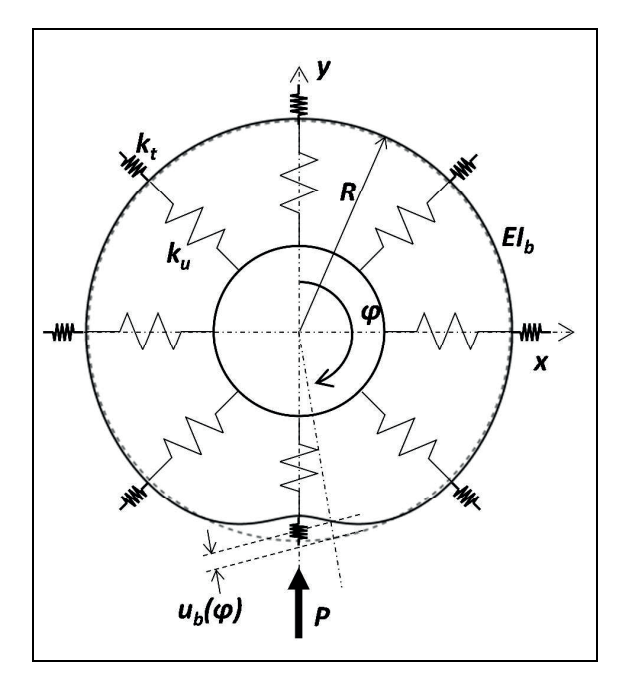


Figure 17. Flexible ring model subjected to a point load, adapted from Kim.²⁰

The relationship between bending moment and radial deformation of radial arc says

$$M = -\frac{EI_b}{R^2} \left(\frac{\partial^2 u_b}{\partial \varphi^2} + u_b \right) \tag{17}$$

With assuming static equilibrium for an infinitesimal element of the circular beam in combined with equation (17), the equation for the tread band deformation can be written as the following equations referring to²⁰

$$\frac{d^5 u_b}{d\varphi^5} + \frac{2d^3 u_b}{d\varphi^3} + \lambda_b \frac{du_b}{d\varphi} = 0$$
 (18)

where

$$\lambda_b = \sqrt{\frac{R^4 k_u}{EI_b} + 1} \tag{19}$$

Equation (20) is the analytical solution to equation (18) with the boundary conditions: zero slopes at $\varphi = 0$, $\varphi = \pi$, equilibriums of shear forces and external forces at $\varphi = 0$, $\varphi = \pi$, and no rotational movement of the ring

$$u_{(b)r\varphi}(\varphi) = P(\bar{C}_0 + \bar{C}_1 \cosh(\alpha \varphi) \cos(\beta \varphi) + \bar{C}_4 \sinh(\alpha \varphi) \sin(\beta \varphi))$$
(20)

in which

$$\bar{C}_0 = \frac{R^3}{2EI_b\pi\lambda_b^2} \tag{21}$$

$$\bar{C}_{1} = \frac{R^{3}(\alpha \cosh(\pi \alpha) \sin(\pi \beta) + \beta \cos(\pi \beta)\alpha \sinh(\pi \alpha))}{2EI_{b}\alpha\beta(\alpha^{2} + \beta^{2})(\cos(2\pi \beta) - \cosh(2\pi \alpha))}$$
(22)

$$\bar{C}_4 = \frac{R^3(\beta \cosh(\pi \alpha) \sin(\pi \beta) - \alpha \cos(\pi \beta) \alpha \sinh(\pi \alpha))}{2EI_b \alpha \beta (\alpha^2 + \beta^2) (\cos(2\pi \beta) - \cosh(2\pi \alpha))}$$
(23)

where

$$\alpha = \sqrt{\frac{\lambda_b - 1}{2}}, \beta = \sqrt{\frac{\lambda_b + 1}{2}}$$

For the deflection of the tire subjected to distributed contact pressure, $u_b(\varphi)$ is determined by integrating equation (15)

$$u_b(\varphi) = \int_{\pi - \varphi_c}^{\pi + \varphi_c} p(\varphi_p) \bar{u}_b(\varphi; \varphi_p) R d\varphi_p$$
 (24)

in which $p(\varphi_p)$ is the contact pressure distribution along the contact length, φ_c is contact angle, and $\bar{u}_b(\varphi;\varphi_p)$ is the radial deformation of the ring at φ contributed by $p(\varphi_p)$, which can easily be obtained by shifting the solution function, equation (20), by φ_p . Thus, since tire parameters and pressure distribution are known, the radial deformation of the tread band can be calculated analytically.

To solve the contact problem using the ring model, the same contact model as presented in Section 3.2 was used. The pressure distribution was calculated by multiplying the tread deformation (u_b-u_r) by its stiffness (k_t) (refer to Figure 13)

$$p(\varphi) = k_t(u_b(\varphi) - u_r(\varphi)) \tag{25}$$

By substituting equation (25) into equation (24) and integrating, $u_b(\varphi)$ can be found. To solve this equation, it was discretized as is shown in equation (26)

$$u_b(\varphi) = \sum_{i=1}^{N_{\varphi}} [k_t(u_b(\varphi) - u_r(\varphi))] \bar{u}_b(\varphi; \varphi_{pj}) R \Delta \varphi \qquad (26)$$

where N_{φ} is the number of elements within the contact patch and $\Delta \varphi$ is the incremental angle for discretization. Simplifying, equation (21) is expressed as

$$k_t \bar{U}(u_b - u_r) R \Delta \varphi = u_b \tag{27}$$

In this expression, φ ranging between $[0\ 2\pi]$ is discretized into $\varphi_1, \varphi_2, ..., \varphi_{Nt}$, where N_t is number of discretized points and is determined by dividing 2π by $\Delta \varphi$. u_b and u_r are N_t X 1 vectors for tread band and total tire deformation, respectively. \overline{U} has $N_T \times N_{\phi}$ dimension and its (i, j) element is $\bar{u}_b(\varphi_i; \varphi_{pi})$.

By collecting equation (27) for u_b , the following equation is obtained

$$\boldsymbol{u_b} = \left(\bar{\boldsymbol{U}} - \frac{1}{k_t R \Delta \varphi} \boldsymbol{I}\right)^{-1} \bar{\boldsymbol{U}} \boldsymbol{u_r} \tag{28}$$

Using equation (28), ring deformation can be obtained. However, the contact angle φ_c is still unknown. This is determined through the iterative procedure until the two tread deformation constraints are satisfied. First, the tread rubber cannot be stretched, in other words, the pressure from equation (25) must be positive. Second, the tread rubber cannot be compressed into zero or negative thickness as discussed in Gong.¹⁷ This constraint can be mathematically written as

$$0 < u_b(\varphi) - u_r(\varphi) < \tau \tag{29}$$

where, τ is the tread thickness and $u_r(\varphi) = d_0 - R_0(1 - \cos(\pi - \varphi))$ from equation (13).

Usually, the second constraint is satisfied when realistic tire parameters are used. Therefore, first constraint is the only one which must be satisfied through the iterative process. This iterative process continues until all of the points in the contact patch meet this constraint and contact angles are found. The stiffness parameters, EI, k_u , and k_t are determined by using the error minimization method between estimated vertical load and the applied vertical load, which is the same approach suggested by Kim.²⁰

Solving the contact problem using strain measurement

The shape of the radial deformation of the ring is dominated by the applied pressure distribution. In this suggested method, the profile of contact pressure was adjusted so that the radial deformation from the flexible ring model (which doesn't have tread elements) can be fitted to that estimated from strain measurements. On the contrary, in the conventional contact problem, the pressure distribution is identified using the tire-road contact model during the numerical solution. For the purpose of representing arbitrary shapes of pressure profiles, a numerical model was proposed as shown in equation (30)

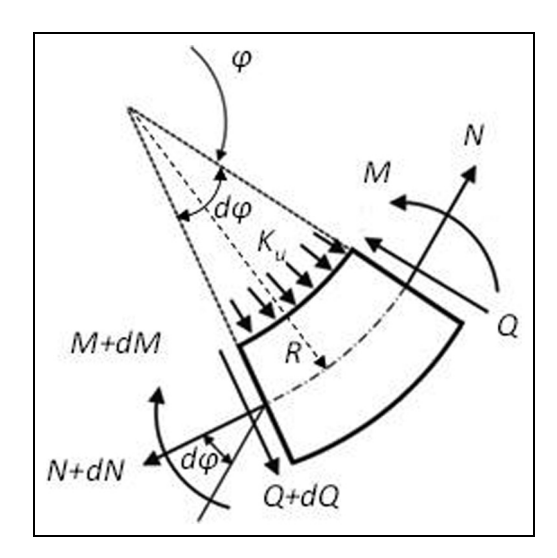


Figure 18. Force equilibrium diagram for infinitesimal element of curved beam.

$$p(x) = p_0 \left(1 + S \left(x \frac{a_1 + a_2}{2} \right) \right)$$

$$\left((x - a_1)(x - a_2) \left(\frac{S_f}{5000} + \left(x - \frac{a_1 + a_2}{2} \right)^2 \right) \right)^{\frac{1}{n_p}}$$
(30)

where a_1 and a_2 are contact length in (m) from the center to leading and trailing edges, respectively; S is the shape factor for the asymmetric distribution; and S_f and n_p are shape factors for diverse curvatures in the pressure distribution

$$p_0 = F_z / \int_{a_1}^{a_2} \left(1 + S \left(\varphi - \frac{a_1 + a_2}{2} \right) \right)$$
$$\left((x - a_1)(x - a_2) \left(\frac{S_f}{A} + \left(x - \frac{a_1 + a_2}{2} \right)^2 \right) \right)^{\frac{1}{n_p}}$$

In this study, only symmetric pressure distributions are assumed, so the shape factor S is set to zero. Figure 19 illustrates the effects of n_p and s_f on pressure distribution shapes. a_1 and a_2 are known form the peak-to-peak values of the strain rates and p_0 can also be calculated once other shape parameters are set under known load, F_z . Thus, only S_f and n_p need to be determined through the optimization process which tries to minimize the difference between the radial deformations identified from the strain measurements and calculated by the flexible ring model.

The stiffness parameters for this ring model cannot be directly measured since they are pressure and load dependent and have different layers. Identifying these values is a challenging task. In this article, these parameters were determined through the optimization

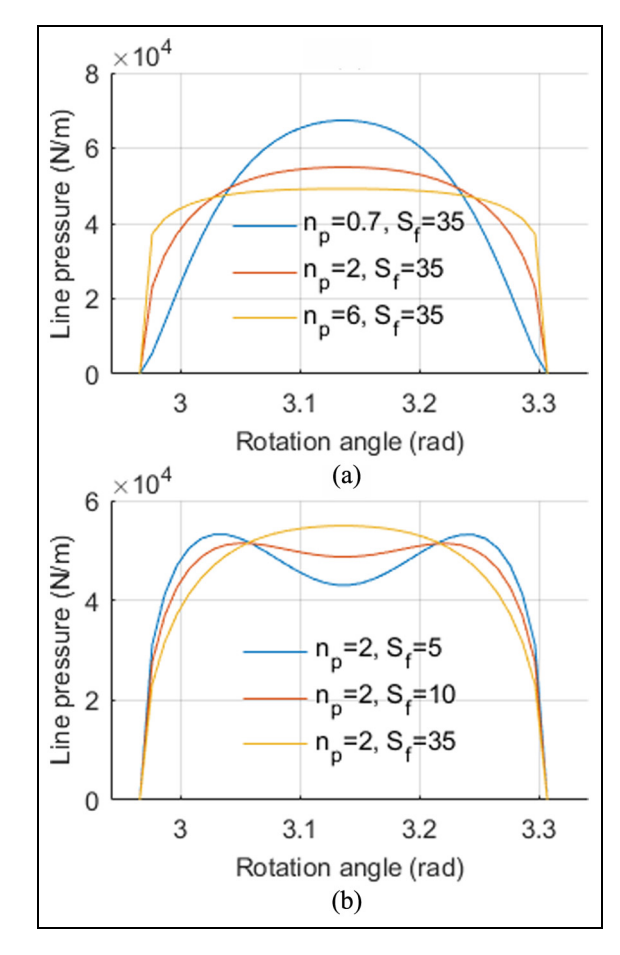


Figure 19. Realization of one dimensional pressure distribution for diverse shape factors: (a) effects of n_p and (b) effects of S_f .

process. The optimization formula to identify the pressure distribution and model parameters is written as follows

Find
$$EI_b, k_u, n_p, s_f$$
, such that Min.
$$\sum_{i=1}^{5} \bar{u}_{Sim}^{(i)} - \bar{u}_{FDM}^{(i)} 2$$

where \bar{u}_{FDM} is known value from strain measurements by FDM, \bar{u}_{Sim} can be calculated by using equation (28), and i represents the different test loads. The tire parameters and shape factors, (EI_u, k_u, n_p, s_f) , are design variables in this optimization scheme. EI_u is assumed to be constant over the entire load range, whereas k_u has the load dependency as suggested in²¹

$$k_u = Ae^{Bd_0} (31$$

Therefore, using this methodology, the pressure distribution and tire parameters can be estimated based on the combination of the flexible ring model and strain measurements.

Simulation results and validation

To validate the proposed method based on strain measurements, strains at the tire innerliner for three

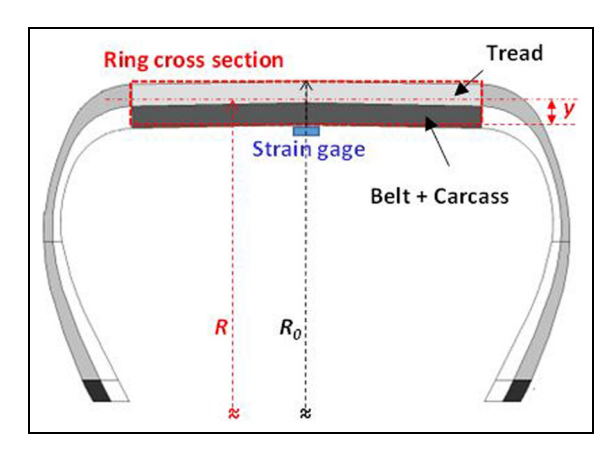


Figure 20. Geometrical parameters of tire for simulation.

Table 2. Geometrical tire parameters.

R ₀ (m)	Spec A	Spec B	Spec D	
	0.374	0.374	0.375	
R (m)	0.362	0.362	0.363	

different tires were measured. These tires had the same specifications except for the belt constructions: LTR belt with 27° belt angle (spec A), PCR belt with 27° belt angle (spec B), and PCR belt with 30° belt angle (Spec D). Geometrical parameters (R, R_0, R_l) and stiffness parameters (EI_b, k_u, k_t) were needed for this simulation. Loaded rolling radius, R_b , was measured on the Flat-Trac test rig. Unloaded radius of tire, R_0 , was determined by extrapolating the loaded rolling radius at zero test load. The radius of the ring, R, is the distance between wheel center and neutral plane of the circular bream. R_0 , R, and y are shown in Figure 20. y is determined such that the position of the neutral axis is located at the first belt position as discussed in Section 3.1 but slightly adjusted for different tests in order to match the simulated strain to the measured strain, which slightly varies among test runs, even for the same tire. The parameter values used are shown in Table 2.

Figure 21 compares the radial deformations from the proposed method using optimization (shown as

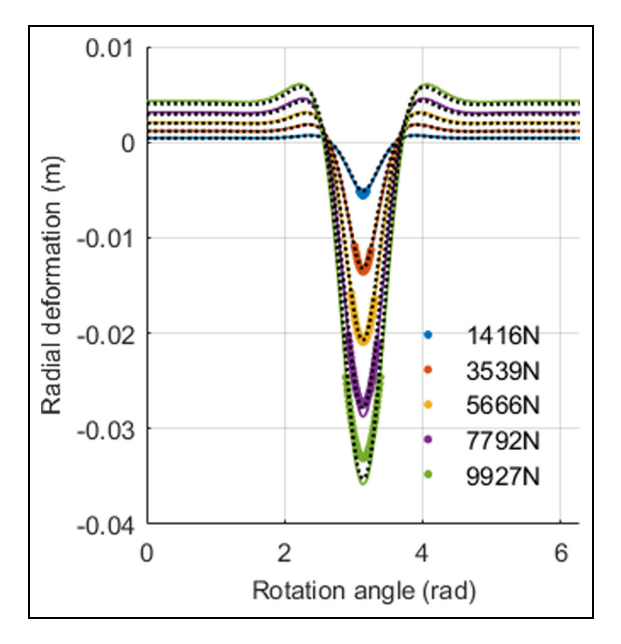


Figure 21. Radial deformations estimated by different methodologies: based on flexible ring model, strain measurement, and optimization.

"from opti." in Figure 21), from the conventional method using the flexible ring model (shown as "from model" in Figure 21) and identified from real strain measurements using FDM (shown as "from strain" in Figure 21).

The proposed method results agree well with the conventional method. However, they both show discrepancies when compared to the one estimated from measurement at the highest load. The new and conventional methods use the same flexible ring model, and it might not represent the tire deformation properly under higher loads, that is, the deflection becomes large. The tire models used in simple and static methods did not include the circumferential elements of the sidewall, frictional effects between the tire and the road, nor the shear tread deformation. More discussions on this will be delivered later.

Figure 22 presents the contact length obtained from various methods. Static footprints ("F/P test" in

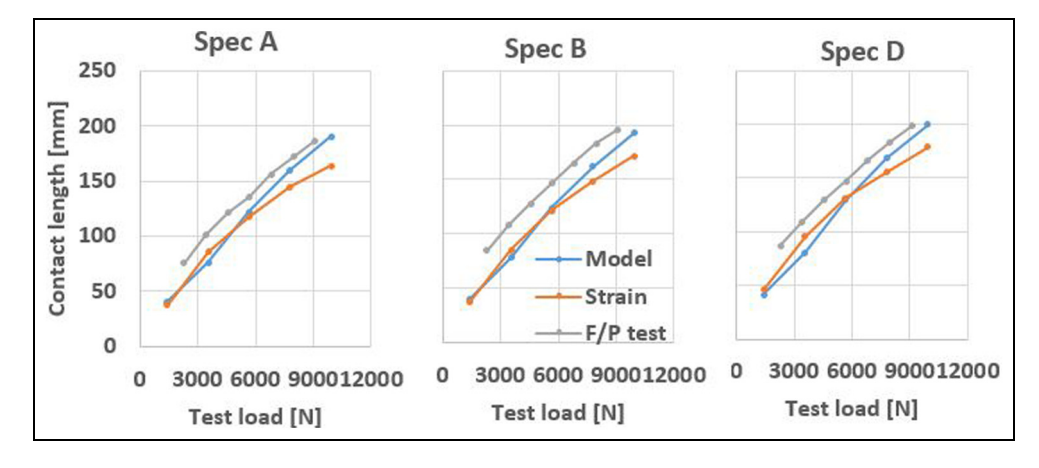


Figure 22. Comparison of contact lengths obtained from different methodologies.

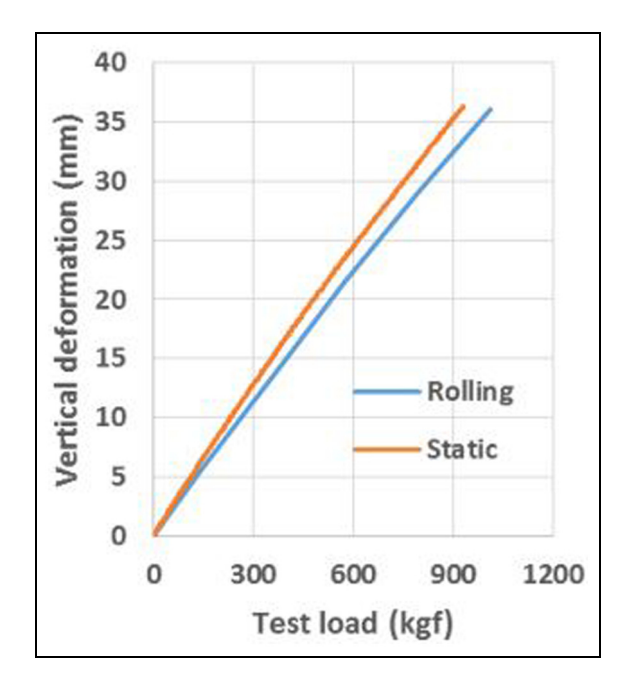


Figure 23. Vertical deformations versus test load for rolling and static tire.

Figure 22) were measured on the indoor static test rig at somewhat different test loads but the entire range of test loads overlap with those of the Flat-Trac test making comparisons possible. The center contact length from the foot print test was chosen for the comparison with the other methods.

The measured contact lengths are always longer than the estimated ones. When it comes to the flexible ring model simulation ("Model" in Figure 22), the main input parameter is the vertical deformation of the loaded tire. This deformation was measured on the Flat-Trac test rig at 65 km/h. The vertical stiffness of the rolling tire is expected to be higher than that of the static tire because the dynamic modulus of the rubber is higher, making the rolling tire stiffer. Figure 23 compares the vertical deformations as a function of the test load; one was measured on the static test rig; the other on the Flat Trac test rig.

The shorter contact length due to higher vertical stiffness of the rolling tire would be compensated by the slippery road surface assumed in the model (no frictional force), since the slippery road surface tends to contribute to longer contact lengths. It is observed that the contact length from simulation ("Model" in Figure 22) increases rapidly as the test load is increased. As the test load increases, the frictional force also increases which makes the contact length increase less as observed in the other cases ("FP test" and "Strain" in Figure 22). The contact length estimated from the strain measurement ("Strain" in Figure 22) shows similar load dependency to the footprint measurements. The shorter contact length from this method can be explained by the dynamic stiffening effect since strain

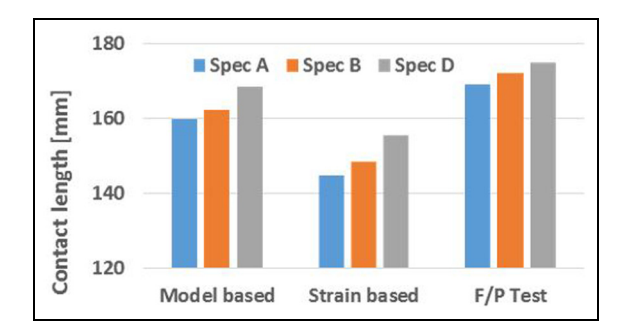


Figure 24. Comparison of contact lengths at reference test load for different tire specifications.

was also measured inside the rolling tire. Moreover, the centrifugal effect of the rolling tire causes the tire to "lift" vertically away from the road surface at higher speeds.

Figure 24 compares the contact lengths of different tires obtained from different methods. Center contact lengths at the reference load are compared. For all cases, Spec D has the longest contact length, whereas Spec A has the shortest. All methods demonstrate the expected trend when the belt stiffness varies from stronger (Spec A) to weaker (Spec D). However, the contact length for Spec D is slightly longer than other specs when contact lengths are measured on the static foot print test rig, whereas it is much longer when estimated from strain measurements. This phenomenon could be due to the difference in contact features between the rolling and static tires, especially when the tire has lower belt stiffness (Spec D).

Figure 25 shows the estimated stiffness parameters from the flexible ring model which includes the optimization with strain measurements. Both identification methods deliver the same ranking for EI_b : Spec A > Spec B > Spec D. This can be expected based on the belt construction of each tire. However, sidewall stiffness is almost the same regardless of estimation methods and tire specs because the tires only differ in the belt construction. However, it was noticed that the sidewall stiffness seems less influential in the objective function because it varied less from the initial value during the optimization process. The validity of the sidewall stiffness estimation should be repeated using tires with sufficiently different sidewall stiffness.

One dimensional pressure distribution for both methods are shown in Figure 26: Figure 26(a) is the result of the flexible ring model and Figure 26(b) from the optimization method based on strain measurements. Both of them show typical tendency that the pressure distribution changes from convex to concave shape as test load increases, which was also discussed in Kim. The strain-based method showed more dramatic curvature change.

Figure 27 compares the pressure distribution of each tire estimated from both methods at the reference test

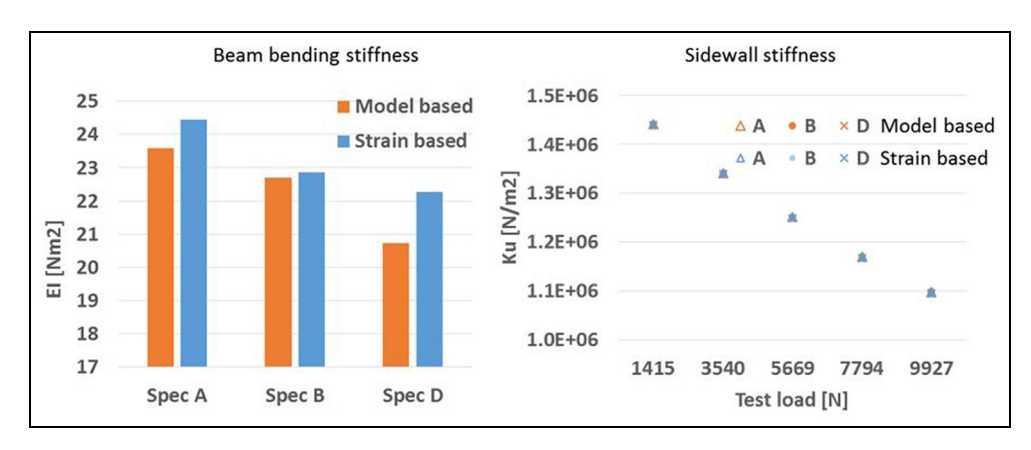


Figure 25. Estimated stiffness parameters for different tire specifications using different methodologies.

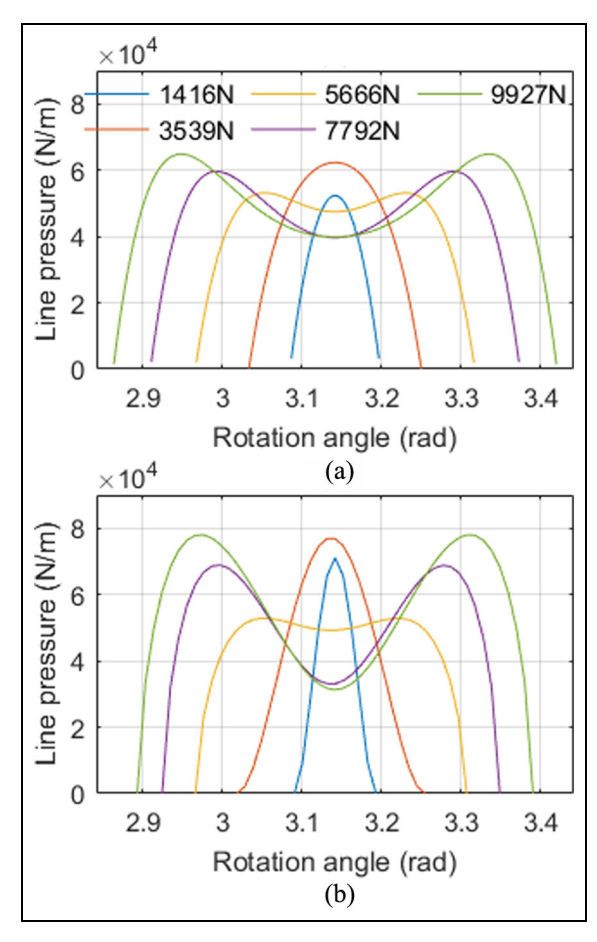


Figure 26. Estimated one dimensional pressure distribution under different test loads: (a) based on flexible ring model only and (b) based on optimization results (flexible ring model + strain measurements).

load. As observed from the comparison of contact lengths, Spec A shows the highest pressure distribution, whereas the lowest one is observed for Spec D, regardless of the estimation method used.

Further validation is needed to secure the strainbased estimation method for contact lengths and contact pressure distribution with a specially designed test

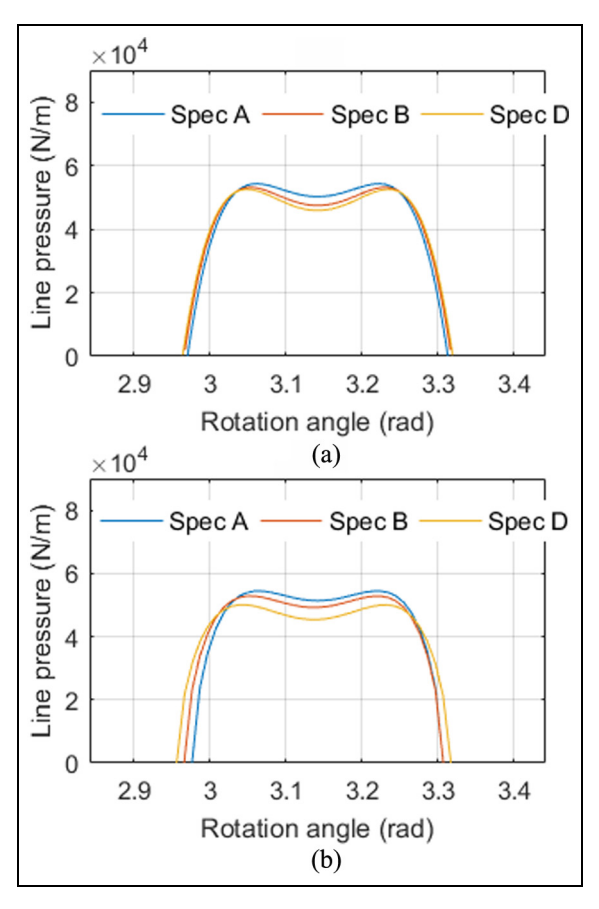


Figure 27. Estimated pressure distributions at reference test load for different tire specifications: (a) based on flexible ring model only and (b) based on optimization results (flexible ring model + strain measurements).

device or FEM simulation, which can deliver the contact features of the rolling tire at high speeds.

Discussion

Figure 28(a) presents measured strains and Figure 28(b) and (c) show the calculated strains based on radial deformations using conventional method and the

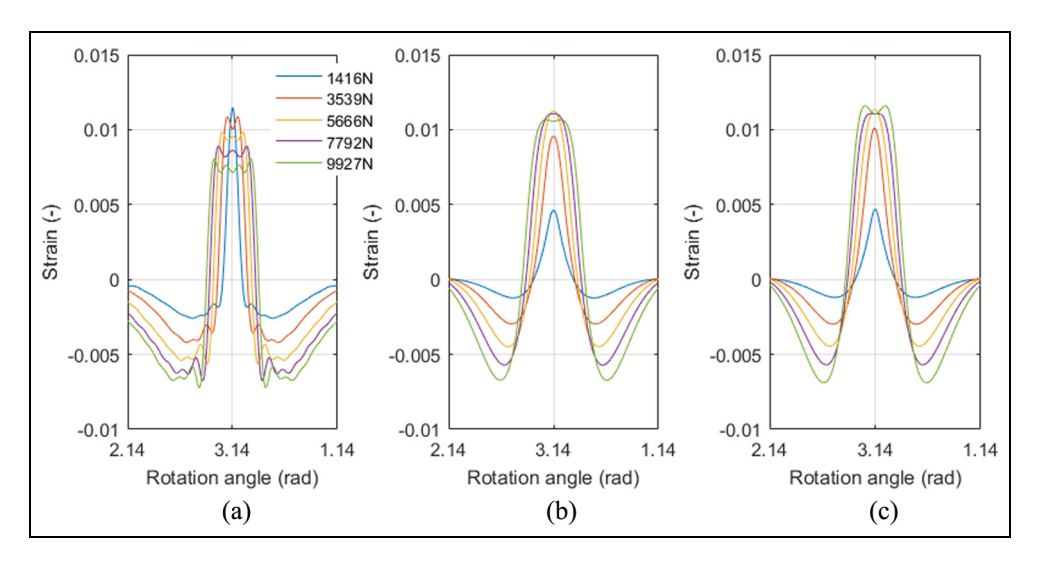


Figure 28. Circumferential strains from simulation and measurements: (a) measured strain, (b) simulated strain from conventional flexible ring contact model, and (c) simulated strain from new method using strain measurements.

proposed method, respectively. Comparing the experimental measurements with the simulated strains from both methods, they share the same features as the experimental data when test load increases. The peak compression and the width of strain response curve increase consistently as the test load increase. However, discrepancy is observed when it comes to the tension in the contact region. In the experimental data, the tension in the contact area monotonically decreases as the test load increases, whereas simulation results present increasing tension when test load increases, specifically from 1416 N to 5562 N. Diverse factors can contribute to this disagreement, but the most likely cause is the nonexistence of friction between the tread and the road surface in the simulation.

Figure 29 shows FEM simulation results of circumferential strains calculated at the innerliner for a 215/60R16 size tire. Although the tire of FEM model is different from the tires used in this study, simulation results show the general effects of the frictional force on circumferential strains. The upper chart shows the simulation results when the static tire is subjected to a vertical load on the frictional surface with the friction coefficient of 0.5. The same simulation is repeated with the coefficient of zero, and the results are shown in the lower chart. Comparing both, it is clear that the results which includes friction have more similar features to experimental data; as the test load increases, the tension in the contact region decreases

Figure 30 explains the effects of frictional force on circumferential strains. The frictional force causes tips of the tread elements adhering to the road surface to move outward in the circumferential direction. This leads to bending deformation of tread elements inducing compressive horizontal forces in the tire inner layers. As a result, the tension induced from the bending motion of the ring is slightly reduced in the contact region.

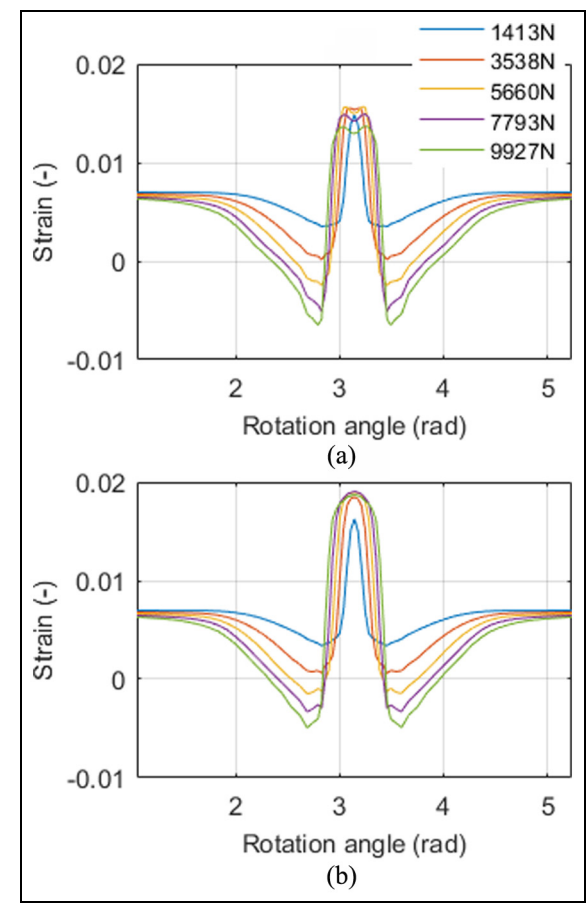


Figure 29. FEM simulation results for circumferential strains.

It should also be mentioned that even though the optimization results of the suggested method for the radial deformation are very close to those estimated from strain measurements as presented in Figure 21, there are still considerable differences in the case of strains. This indicates that the strains are very sensitive

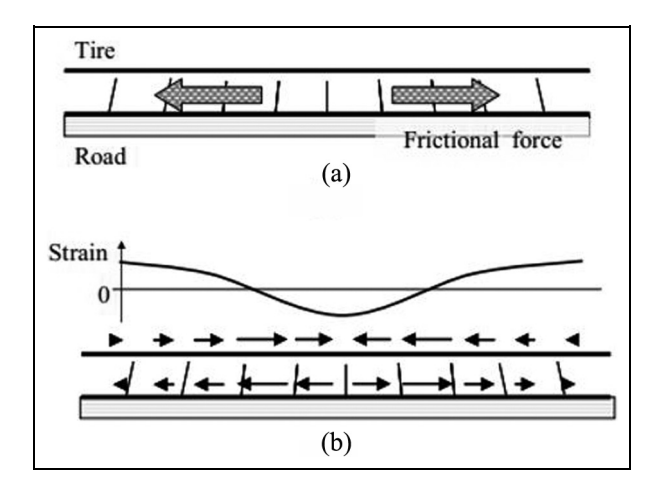


Figure 30. Cross-sectional deformation and strain distribution of a tire derived from the static frictional force: (a) the applied load and (b) the strain distribution.⁹

to the shape of the radial deformation because they depend on the first and second derivative of the radial deformation on φ . Thus, if the model is not complete enough to describe the real strains of the tire, utilizing the radial deformation is a more effective way to identify tire characteristics as presented here rather than trying to fit the simulated strains directly to the measured ones.

Conclusion

In this study, a new methodology is proposed in order to solve the circumferential tire-road contact problem and estimate related tire parameters by use of the strain-based intelligent tire, where strains are measured at the innerliner.

This study demonstrated the possibility of identifying the tire characteristics using the strain-based intelligent tire. By using the suggested method, it is possible to remove the tread-road contact model of the flexible ring, which cause numerical difficulties and convergence problems. Also, it is expected that tire parameters estimated based on the strain measurement represent real tire characteristics better because strains can be measured inside the rolling tire on the real road surface.

However, the flexible ring model needs to be developed further to include the frictional effects to explain the features of measured strains more closely especially for higher test loads. Also, experimental measurements of the footprint features of a rolling tire at high speeds are required to confirm the validity of the proposed identification method.

This approach can be further advanced by including the braking/acceleration force effects into the model. Strain measurements of the braking/accelerating tire can be understood better using the upgraded flexible ring model. And then, a similar approach as suggested here can be used to characterize tire properties related to the longitudinal forces.

Acknowledgements

All experimental data described in this article were provide by RandD center, Hankook Tire Co. Ltd., Korea.

Declaration of conflicting interests

The author(s) declared no potential conflicts of interest with respect to the research, authorship, and/or publication of this article.

Funding

The author(s) received no financial support for the research, authorship, and/or publication of this article.

ORCID iD

Hojong Lee (D) https://orcid.org/0000-0002-0206-5401

References

- Braghin F, Brusarosco M, Cheli F, et al. Measurement of contact forces and patch features by means of accelerometers fixed inside the tire to improve future car active control. *Vehicle Syst Dynam* 2006; 44: 3–13.
- Morinaga H, Wakao Y, Hanatsuka Y, et al. The possibility of intelligent tire (technology of contact area information sensing). In: *Proceedings of 31st FISITA world automotive* congress, Yokohama, Japan, 22–27 October, 2006.
- Nagaya G. Method for estimating tire slip angle and a tire with sensors mounted therein. US20090055040A1 Patent, 2006.
- 4. Jo HY, Yeom M, Lee J, et al. Development of intelligent tire system. SAE technical paper 2013-01-0744, 2013.
- Yang X, Olatunbosun O, Ramos DG-P, et al. Experimental investigation of tire dynamic strain characteristics for developing strain-based intelligent tire system. SAE Int J Passeng Cars: Mech Syst 2013; 6: 97–108.
- Yang X, Olatunbosun O, Garcia-Pozuelo D, et al. FE-based tire loading estimation for developing strain-based intelligent tire system. SAE technical paper 2015-01-0627, 2015.
- 7. Matsuzaki R and Todoroki A (eds). Intelligent tires for improved tire safety based on strain measurements. In: *Proceedings of the SPIE smart structures and materials, nondestructive evaluation and health monitoring*, San Diego, CA, 8 April 2009. Bellingham, WA: SPIE.
- Matsuzaki R, Kamai K and Seki R. Intelligent tires for identifying coefficient of friction of tire/road contact surfaces using three-axis accelerometer. Smart Mater Struct 2014: 24: 025010.
- Matsuzaki R, Hiraoka N, Todoroki A, et al. Analysis of applied load estimation using strain for intelligent tires. J Solid Mech Mater Eng 2010; 4: 1496–1510.
- Savaresi SM, Tanelli M, Langthaler P, et al. New regressors for the direct identification of tire deformation in road vehicles via "in-tire" accelerometers. *IEEE T Contr Syst Technol* 2008; 16: 769–780.
- 11. Erdogan G, Hong S, Borrelli F, et al. Tire sensors for the measurement of slip angle and friction coefficient and their use in stability control systems. *SAE Int J Passeng Cars: Mech Syst* 2011; 4: 44–58.

12.	Pacejka H.	Tire	and	vehicle	dynamics.	Amsterdam:	Else-
	vier, 2005.						

- 13. Hong S, Erdogan G, Hedrick K, et al. Tyre–road friction coefficient estimation based on tyre sensors and lateral tyre deflection: modelling, simulations and experiments. *Vehicle Syst Dynam* 2013; 51: 627–647.
- Yamagishi K and Jenkins J. The circumferential contact problem for the belted radial tire. *J Appl Mech* 1980; 47: 513–518.
- 15. Yamagishi K and Jenkins J. Singular perturbation solutions of the circumferential contact problem for the belted radial truck and bus tire. *J Appl Mech* 1980; 47: 519–524.
- 16. Jenkins JT. The circumferential contact problem for the belted radial passenger car tire. *Vehicle Syst Dynam* 1982; 11: 325–343.
- 17. Gong S. *A study of in-plane dynamics of tires*. Delft: Delft University of Technology, 1993.
- 18. Kim S-J and Savkoor AR. The contact problem of inplane rolling of tires on a flat road. *Vehicle Syst Dynam* 1997; 27: 189–206.
- 19. Richards R Jr. *Principles of solid mechanics*. Boca Raton, FL: CRC Press, 2000.
- 20. Kim S. *A comprehensive analytical model for pneumatic tires*. Tucson, AZ: The University of Arizona, 2002.
- 21. Mousseau C and Clark S. An analytical and experimental study of a tire rolling over a stepped obstacle at low velocity. *Tire Sci Technol* 1994; 22: 162–181.

EI_b	Bending stiffness of flexible ring (Nm ²)
F_z	Test load (N)
k_u	Sidewall stiffness in the radial direction
	(N/m^2)
k_t	Tread stiffness in the radial direction (N/m^2)
$p(\varphi)$	One dimensional pressure distribution
	along φ (N/m)
P	Point load applied to the tire in the radial
	direction (N)
R	Radius of undeformed flexible ring (tread
	band) (m)
R_0	Overall radius of tire. $R_0 = R + \tau$ (m)
R_{l}	Loaded radius of tire (m)
$u_b(\varphi)$	Radial deformation of flexible ring at
	natural axis (m)
$u_r(\varphi)$	Total tire deformation along φ (m)
y	Radial distance from the neutral axes to a
	particular point (m)
au	Tread thickness (m)
$oldsymbol{\epsilon}_{arphi}$	Circumferential strain at an arbitrary
,	point of flexible ring
φ	Wheel rotation angle (rad)
$\varphi_{c,l}(\varphi_{c,l},$	Contact angle (rad), (Leading and trailing
$\varphi_{c,\ t}$	contact angle (rad))
, -, */	~ ` //

Appendix I

Notation

 d_0 Overall tire deflection (m)